ACS APPLIED MATERIALS & INTERFACES

Energy, Environmental, and Catalysis Applications

Super Large Sn1-xSe Single Crystals with Excellent Thermoelectric Performance

Min Jin, Xiao-Lei Shi, Tianli Feng, Weidi Liu, Haifeng Feng, Sokrates T. Pantelides, Jun Jiang, Yunxia Chen, Yi Du, Jin Zou, and Zhi-Gang Chen

ACS Appl. Mater. Interfaces, **Just Accepted Manuscript** • DOI: 10.1021/acsami.8b21699 • Publication Date (Web): 05 Feb 2019

ACS Publications

is published by the American Chemical Society. 1155 Sixteenth Street N.W., Washington, DC 20036

Super Large $Sn_{1-x}Se$ Single Crystals with Excellent Thermoelectric Performance

Min Jin[,a,b,1], Xiao-Lei Shi[c,1], Tianli Feng[d,e], Weidi Liu[c], Haifeng Feng[f], Sokrates T. Pantelides[d,e], Jun Jiang[b], Yunxia Chen[a], Yi Du[f], Jin Zou[*,c,g], and Zhi-Gang Chen[*,h,c]*

[a] College of Materials, Shanghai Dianji University, Shanghai 201306, P R China

[b] Ningbo Institute of Materials Technology and Engineering, Chinese Academy of Sciences, Ningbo 315201, P R China

[c] Materials Engineering, University of Queensland, Brisbane, QLD 4072, Australia

[d] Department of Physics and Astronomy and Department of Electrical Engineering and Computer Science, Vanderbilt University, Nashville, Tennessee 37235, USA

[e] Center for Nanophase Materials Sciences (CNMS), Oak Ridge National Laboratory, Oak Ridge, Tennessee 37831, USA

[f] Institute for Superconducting and Electronic Materials (ISEM), Australian Institute for Innovative Materials (AIIM), University of Wollongong, Wollongong, NSW 2500, Australia

[g] Centre for Microscopy and Microanalysis, University of Queensland, Brisbane, QLD 4072, Australia

[h] Centre for Future Materials, University of Southern Queensland, Springfield, QLD 4300, Australia

Keywords: Thermoelectric, Tin selenide, Single crystal, Characterizations, First-principle calculations

ABSTRACT

SnSe single crystals have drawn extensive attention for their ultra-low thermal conductivity and outstanding thermoelectric performance. Here, we report super large $Sn_{1-x}Se$ single crystals with excellent thermoelectric properties, fabricated *via* an advanced horizontal Bridgman technique with a great yield and high-reproducibility. The obtained single crystals have a super large size of ~70 mm×50 mm×15 mm with a considerable weight of 148 g, which leads to a record-high mass density >6.1 g cm^{-3}. Extensive chemical characterization demonstrates that ~0.3 % Sn vacancies are present, which results in a large concentration of holes, ~1.2×10^{19} cm^{-3}, and an enhanced power factor of ~6.1 μW cm^{-1} K^{-2} at 793 K. Simultaneously, the Sn vacancy-induced lattice distortions result in a low thermal conductivity of ~0.39 W m^{-1} K^{-1} at 793 K, leading to a competitive *ZT* of ~1.24. This work demonstrates that large-size off-stoichiometric SnSe single crystals hold promise to achieve high thermoelectric performance.

1. INTRODUCTION

By offering a direct, quiet, and convenient conversion between electricity and thermal energy, thermoelectric materials are in principle able to provide a sustainable solution to the challenges of excessive energy consumption and environmental problems.[1-3] The efficiency of such direct energy conversion is evaluated by the dimensionless figure of merit $ZT = S^2\sigma T/\kappa$,[4] where σ, S, $S^2\sigma$, T and κ are the electrical conductivity, Seebeck coefficient, power factor, absolute temperature, and thermal conductivity,[5-6] respectively. κ can be considered as the sum of κ_e and κ_l,[7] namely the electronic and lattice contributions,[8] respectively. To achieve a high ZT, it is necessary to control the carrier concentration n to optimize the $S^2\sigma$.[9] At the same time, a low κ_l is essential.[10] To date, electron band structure and vibrational structure engineering have been two major strategies to achieve high $S^2\sigma$ and low κ_l.[11]

As a typical semiconductor with low cost, low toxicity and low intrinsic κ, stannous selenide (SnSe) has received extensive attention because of its great potential to achieve high thermoelectric performance.[12] *p*-type SnSe single crystals have shown an ultra-high ZT of ~2.6,[13] owing to their high $S^2\sigma$ and extremely low κ_l along the *b*-axis.[13-14] The single crystals produced *via* advanced Bridgman technique can produce large scale crystals with productivity of ~20 g each time[13] and large size of 13 mm × 15 mm[15]. However, the fabrication of SnSe single crystals are still complex and time-consuming to some extent,[16] and the thermoelectric performance below the phase-transition temperature (800 K) is still not excellent due to the low hole carrier concentration p of $<1\times10^{19}$ cm^{-3} at peak ZT for pure SnSe.[13] Besides, there are critical controversies on the reported ultralow κ in SnSe single crystals at high temperatures (<0.4 W m^{-1} K^{-1}).[17-18] To solve these issues, an improved crystal growth technique with a lower production cost and higher efficiency is required to realize large-size, high-quality SnSe single-crystal production.

Within the advanced crystal growth techniques, the Horizontal Bridgman (HB) method is a recently developed and promising crystal-growth route.[19] Compared to the vertical Bridgman (VB),[13] temperature gradient (TG)[20], and zone-melting (ZM)[21] methods, the HB technique can realize a much larger temperature gradient of ~3 K cm^{-1} and a higher cooling rate of ~25 K h^{-1},[19] enabling us to efficiently fabricate SnSe single crystals at potentially industrial scale. Nevertheless, the achieved single crystals are still not large enough and exhibit micro-cracks.[19] Therefore, they cannot meet the requirement of fabricating thermoelectric devices and need further improvement. Meanwhile, for the strategies of further improving the thermoelectric performance of SnSe, previous studies indicate that inducing Sn vacancies in the SnSe matrix *via* off-stoichiometric design (such as $Sn_{0.98}Se$[9, 22]) can effectively tune p to $>1.2\times10^{19}$ cm^{-3}, compared to $\sim6.7\times10^{18}$ cm^{-3} in stoichiometric SnSe, and realize enhanced ZTs to ~1.0 below 800 K in SnSe crystals.[9, 23-24]. In fact, the vacancies are inherent to SnSe and commonly observed in other chalcogenides and/or conventional thermoelectric materials such as Cu_2Se.[25-26]

In this work, we use an improved HB method to fabricate super large off-stoichiometric SnSe ($Sn_{1-x}Se$) single crystals with competitive-high ZT of ~1.24 below the phase transition temperature of 800 K. **Figures 1(a)** and **1(b)** illustrate the crystal growth technique and the temperature program, respectively, in which we choose B_2O_3 as encapsulant to prevent solution volatilization at high temperature,[3] and use a highly elastic pyrolytic boron nitride (PBN) crucible as lining to further eliminate thermal stress during the crystal-growth process in order to avoid micro-cracks in the fabricated single crystals. The achieved single crystal has a super large size of ~70 mm×50 mm×15 mm with a considerable weight of 148 g, which has a record-high mass density (>6.1 g cm^{-3}), as shown in **Figure 1(c, d)**. To realize off-stoichiometric SnSe single crystals grown by our improved HB method, we refer to the Sn-Se phase diagram (shown in **Figure S1** in Supporting Information) and adjust the stoichiometric ratio of precursors Sn and Se as 0.98:1. Through detailed structural and compositional characterization, including X-ray diffraction (XRD), X-ray photoelectron spectroscopy (XPS), energy dispersive spectroscopy (EDS), and electron probe micro-analyzer (EPMA), we confirm that we realize off-stoichiometric SnSe single crystals. Compared with stoichiometric SnSe,[19] the Sn vacancy level of ~0.3 % results in an improved p of $\sim 1.2\times10^{19}$ cm^{-3} at 793 K, as well as an enhanced $S^2\sigma$ of ~6.1 μW cm^{-1} K^{-2}. The higher Sn vacancy concentration observed in our samples explains why other SnSe single crystals obtained in the literature have different thermoelectric properties from ours.[19, 27-28] In addition, our detailed structural and morphological characterization using scanning electron microscopy (SEM), scanning tunneling microscopy (STM), transmission electron microscopy (TEM) and spherical aberration-corrected scanning TEM (Cs-STEM) confirm the single crystals and indicate that there are lattice distortions caused by Sn vacancies, which can effectively scatter the phonons and result in a low κ of ~0.39 W m^{-1} K^{-1} at 793 K, contributing to a competitive peak ZT of ~1.24 at this temperature.

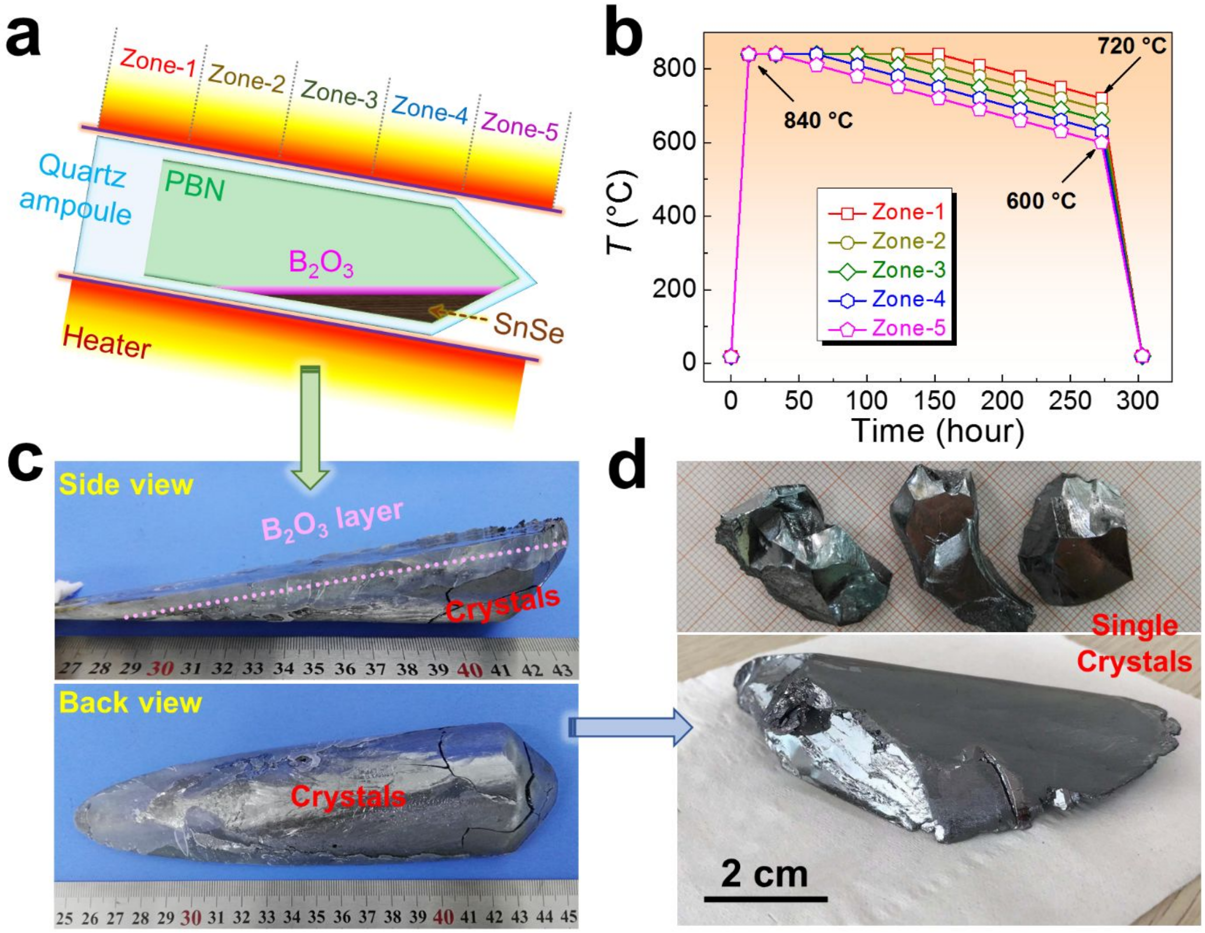

Figure 1. Fabrication of super large $Sn_{1-x}Se$ single crystals. (a) Illustration of Horizontal Bridgman (HB) method; (b) temperature program for $Sn_{1-x}Se$ single crystal growth; (c) side and back view of our synthesized $Sn_{1-x}Se$ single crystals before separation; and (d) achieved $Sn_{1-x}Se$ single crystals.

2. EXPERIMENTAL SECTION.

2.1 Reagents and Synthesis. SnSe single crystals were synthesized by using HB method. High purity Sn (99.999 %) and Se (99.999 %) with mole ratio of 0.98:1 were weighted as precursors (280 g in total). These precursors were loaded in a quartz ampoule (Ø25 mm) and sealed by oxyhydrogen flame after the quartz ampoule was vacuumed to ~10^{-3} Pa. After that, the quartz ampoule was placed into a rocking furnace for synthesis. The furnace temperature was set at 930 °C to guarantee the full reaction of the precursors. After the solution was soaked for 30 minutes, the rocking system was rotated at a rate of 30 r min^{-1} for 0.5 hour to ensure that the synthesis is homogeneous. Finally, the furnace was cooled to room temperature naturally and SnSe polycrystals was obtained. These polycrystals were treated as the precursors of the followed single crystal growth.

SnSe single crystal growth was carried out in a HB furnace. The furnace was composed of five independent heating zones, as shown in **Figure 1(a)**. The above synthesized polycrystalline SnSe together with appropriate B_2O_3 encapsulant were loaded into a 5 N purity elastic pyrolytic boron nitride (PBN) crucible (Ø55 mm with 0.8 mm in thickness), which was also sealed in a quartz ampoule with ~10^{-3} Pa vacuum. The B_2O_3 encapsulant would remain solid state and float on the solution as its melting point is 450 °C and the density was only 2.46 g cm^{-3}. The quartz ampoule was moved into the HB furnace, its shoulder part was adjusted in the location corresponding to Zone 5. To achieve large-scale single crystals, the furnace tube was inclined ~30° to horizontal plane so that most of the solution would stay on the corn part of PBN crucible. **Figure 1(b)** shows the temperature program for SnSe single crystal growth. Within 2 hours, all the zones were heated to 840 °C which was higher than the melting point of $SnSe_2$ but lower than that of SnSe, as shown in Sn-Se phase diagram in **Figure S1**. After the solution was soaked for 35 hours, crystal growth took place from Zone 5 to Zone 1 by decreasing the temperature gradually. The temperature gradient for SnSe crystal growth was about 2-3 °C cm^{-1}. As the temperatures of Zone 5 and Zone 1 were decreased to 600 °C and 720 °C, respectively, all the heating zones were cooled to room temperature simultaneously with a speed of ~30 °C per hour. The as-grown single crystals were obtained by leaching PBN crucible in ~50 °C carbinol (>99.7 %) to dissolve B_2O_3.

2.2 Thermoelectric Properties Measurements. The densities (ρ) of the single crystals were measured by the Archimedes method (DM50, China).[9] The achieved density of ~6.1 g cm^{-3} for $Sn_{1-x}Se$ is slightly lower than the theoretical values of 6.179 g cm^{-3} for SnSe and ~6.162 g cm^{-3} for $Sn_{1-x}Se$ (here $x = 0.003$) due to the experimental error. In our measurements, σ and S were measured simultaneously using a Seebeck coefficient/electric resistivity measuring system (ZEM-3, ULVAC Technologies, Inc.) in the temperature range between 300 and 800 K. The thermal diffusivity D was measured using the laser flash diffusivity method (LFA 457, NETZSCH Group). κ was calculated using $\kappa = D{\cdot}C_p{\cdot}\rho$,[13] where C_p is the specific heat capacity obtained by differential scanning calorimetry (DSC 404 C; NETZSCH Group), and p was measured using the van der Pauw technique under a reversible magnetic field of 1.5 T. To ensure the repeatability of synthesized products and their demonstrated thermoelectric properties, each sample were measured for at least 3 times.

2.3 Characterization. The synthesized single crystals were characterized by XRD (Bruker-D8) to determine their crystal structures by using Cu Kα radiation (λ= 1.5406 Å) at room temperature, and XPS (Kratos Axis Ultra) to determine the Sn and Se valence states in SnSe. The morphological and chemical characteristics of single crystals were investigated using SEM (JSM-6610, JEOL Ltd.), and their structural characteristics were studied using HRTEM (TECNAI-F20) and Cs-corrected HR-STEM (Titan-G2). The TEM specimens of single crystals were prepared by focused-ion-beam technique (FEI Scios Dual-beam System). The EPMA (JEOL JXA-8200) was used to determine their compositions, and the EDS (installed in TECNAI-F20) was used to identify the distribution of the elements. The instrumental error of EMPA is 0.1 %. There were 50 test areas for each sample. The Sn vacancies were characterized by STM (STM1500, Unisoku Co.).

2.4 DFT Calculations. Density functional theory calculations were carried out using the Vienna *Ab initio* Simulation Package (VASP)[29-30] with the projector augmented wave method (PAW)[30] and the generalized gradient approximation of Perdew, Burke and Ernzerhof (GGA-PBE)[31] for the electronic exchange-correlation functionals. The plane-wave energy cutoff is 450 eV. The SnSe unit cell was relaxed with a 6×18×18 Γ-centered k-mesh, and the convergence thresholds of the total energy and the forces on each atom are 10^{-8} eV and 10^{-6} eV $Å^{-1}$, respectively. The relaxed lattice constants are $a = 11.7615$ Å, $b = 4.2062$ Å, and $c = 4.5475$ Å. We constructed 2×4×4 (256 atoms) and 2×5×5 (400 atoms) supercells. The atoms in supercells were relaxed with 3×3×3 Γ-centered k-mesh until the forces of each atom are smaller than 10^{-3} eV $Å^{-1}$. The densities of states were calculated by using 3×3×3 Γ-centered k-mesh with the tetrahedron smearing method. The band structures along high-symmetry directions were calculated by using the Gaussian smearing method.

3. RESULTS AND DISCUSSION

3.1 Structural and Morphological Characteristics. To study the grown SnSe single crystals, we first investigated their structural and morphological characteristics. **Figure 2(a)** shows the XRD pattern of cleavage surfaces from the grown crystals (blue line for the stoichiometric SnSe and red line for the off-stoichiometric SnSe) with inset of optical images. The cleavage surfaces of synthesized single crystals show metallic luster. As shown in **Figure 2(a)**, only 400^* and 800^* diffraction peaks can be observed, which match the room-temperature α-SnSe phase by Standard Identification Card, JCPDS 48-1224, confirming that the SnSe are intrinsic single crystals and the cleavage surfaces are typical (100) surfaces.[9, 12, 16, 24] No secondary phase is detectable, indicating that the single crystals have high purity. **Figure 2(b)** shows the magnified 400^* diffraction peaks. Compared with stoichiometric SnSe, the 400^* diffraction peak from the off-stoichiometric SnSe shifts toward higher angles (2θ), indicating a reduced lattice parameter *a*[9, 16, 32] which is caused by the Sn vacancies.[9] To verify the Sn vacancies, we conduct statistical EDS and EPMA analysis, and the results indicate that the off-stoichiometric SnSe has an average Sn vacancy concentration of ~0.3 %, *i.e.*, its composition is $Sn_{0.997}Se$. **Figure 2(c)** the magnified 800^* diffraction peaks and exhibits similar results. In fact, according to crystal-growth theory,[33] the crystal surfaces with slow growth rate (such as (100)) prior to appear in real crystals, and this is why the (100) surfaces are finally exposed in our super large SnSe single crystals. Previous studies also reported that compared with (010) and (011) surfaces, the (100) surfaces have the lowest surface energy,[34] indicating that (100) surfaces are much easier to form in real single crystals. Further discussion can be found in **Section 2** in Supporting Information.

Because the synthesized $Sn_{1-x}Se$ single crystals result from the selected ratio of precursors Sn and Se (0.98:1), to confirm the valence states of Sn and Se in our single crystals, we performed XPS analysis. **Figure 2(d)** shows the XPS scan in the entire binding energy range, indicating that except for Sn 3*d* and Se 3*d* energy states, there is no energy state from other elements (except C and O). **Figure 2(e)** and **2(f)** also show respectively high-resolution XPS scans for Sn 3*d* and Se 3*d*, in which both Sn and Se exhibit only one valence state (Sn^{2+} for Sn and Se^{2-} for Se), indicating high purity of the SnSe phase.[35] The quantified at. % of Sn and Se is fitted well with the obtained ~0.3 % of Sn vacancies.

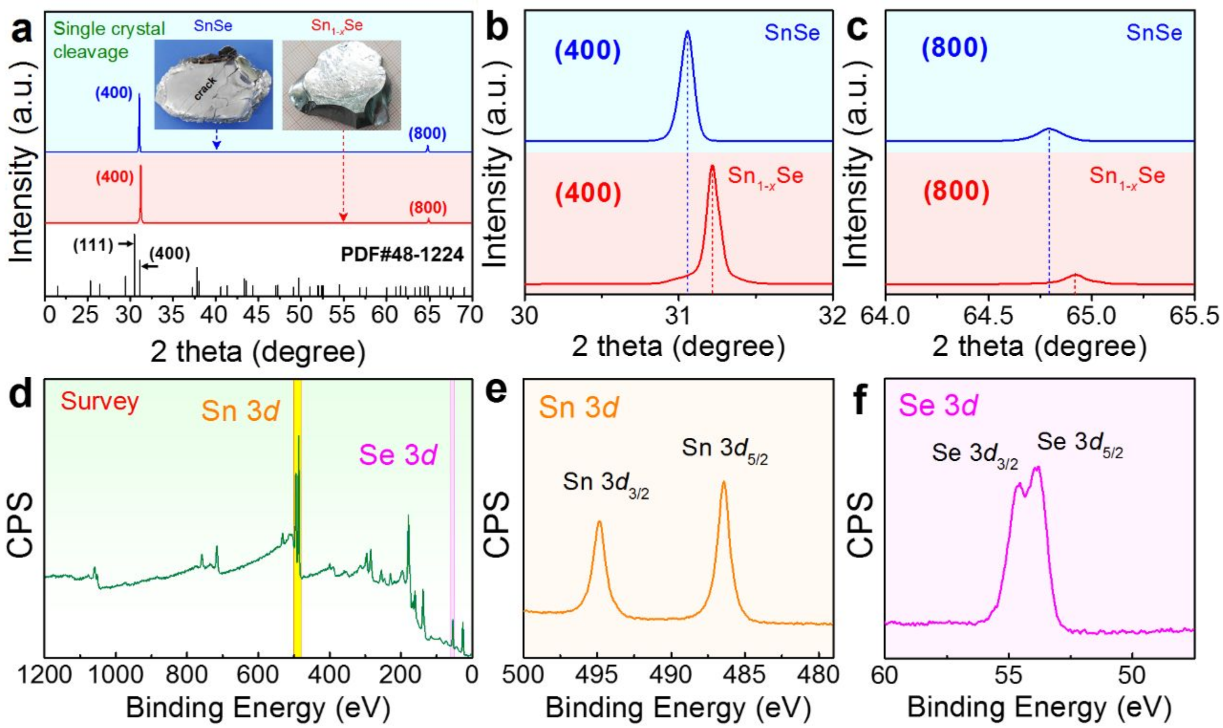

Figure 2. Structural characterizations of synthesized products. (a) XRD results for our SnSe and $Sn_{1-x}Se$ single crystals (on the cleavage surfaces); enlarged (b) 400* and (c) 800* peaks to see the

peak deviation; (d) XPS spectrum of survey scan for the $Sn_{1-x}Se$ single crystals (on the cleavage surfaces); high-resolution XPS scan for (e) Sn 3*d* and (f) Se 3*d*.

Figure 3(a) shows a small piece of SnSe tissue cleaved by a sharp tweezer which is used for the structural and morphological chacterisation. **Figure 3(b)** is the SEM image taken from the cleaved piece of $Sn_{1-x}Se$ single crystal (enlarged from the inset of **Figure 3(a)**), in which cleaved (100) surface of intrinsic $Sn_{1-x}Se$ single crystal can be seen. The inset of **Figure 3(b)** shows the corresponding back-scattering electron (BSE) image, confirming that there is no compositional segregation of either Sn or Se at a microscale. **Figure 3(c)** is an enlarged SEM image, clearly showing that the SnSe layers are cleaved along (100) planes. All these results explain why there are only 400^* and 800^* peaks appearing in the XRD results taken from the cleavage surfaces. **Figure 3(d)** shows the EDS results of the single crystals. The spots were taken from 50 different sites and the maps were taken from **Figure 3(c)**, indicating that both Sn and Se are homogeneously distributed. **Figure 3(e)** is a high-resolution TEM (HRTEM) image, showing slight lattice distortions (as arrows indicate), which are caused by the Sn vacancies.[3] The inset of **Figure 3(e)** shows corresponding selected area electron diffraction (SAED) pattern indexed as typical α-SnSe phase with a (100) surface.[9, 12] **Figure 3(f)** is a high-resolution STM image, showing a typical Sn vacancy.[20, 36-37] **Figure 3(g-i)** are STEM high-angle annular dark field (HAADF) images taken along the [100], [010], and [011] directions, respectively. The overlays in the normal areas show Se atoms in green and Sn atoms in purple and axes, all indicating typical orthorhombic α-SnSe phase.

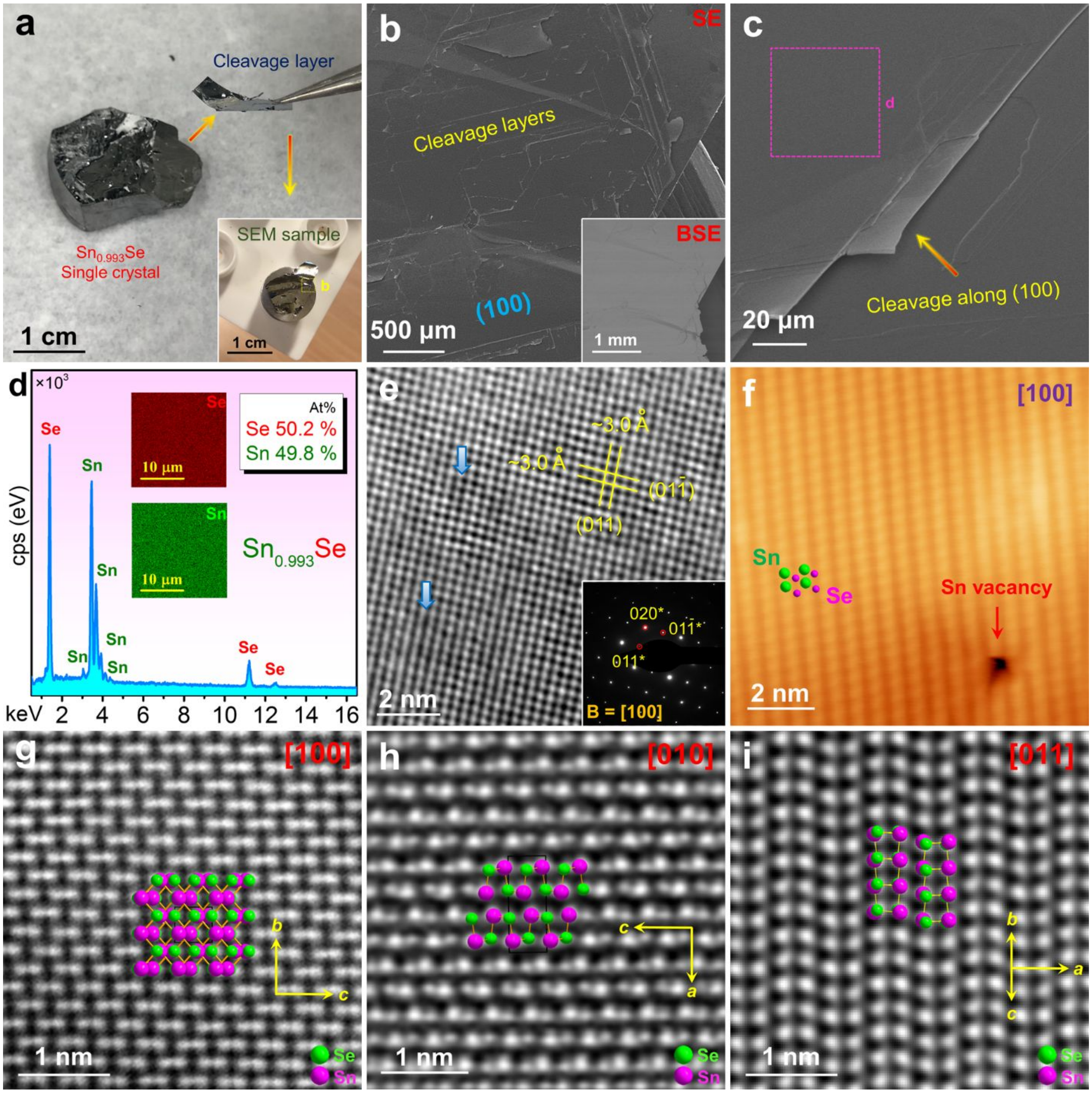

Figure 3. Morphological and compositional characterization of the $Sn_{1-x}Se$ single crystals. (a) SEM sample preparation for $Sn_{1-x}Se$ single crystal and the inset showing the top view of a sample on the holder; (b) SEM image of the $Sn_{1-x}Se$ cleavage surface taken from (a) to show the layered structure and the inset showing the back-scattering electron (BSE) image; (c) magnified SEM image to show the cleavage layers along (100); (d) EDS spot and map results taken from (c) to

show the real composition of $Sn_{1-x}Se$; (e) HRTEM image of the $Sn_{1-x}Se$ cleavage surface to see the lattice distortions as the arrows indicate with inset of corresponding SAED pattern; (f) STM image of the $Sn_{1-x}Se$ cleavage surface to see a typical Sn vacancy; Cs-STEM images of $Sn_{1-x}Se$ taken along the (g) [100], (h) [010], and (i) [011] directions.

3.2 Thermoelectric Performance. To evaluate their thermoelectric performance, we cut and polished the synthesized $Sn_{1-x}Se$ single crystals into regular shapes, as shown in the inset of **Figure 4**. We chose three different $Sn_{1-x}Se$ single crystal samples to investigate their performance stabilities. The stoichiometric SnSe single crystal sample was also investigated for comparison.[19] Since Se can volatilize from SnSe at high temperatures[3] (see our measured thermogravimetric (TG) results shown in **Figure S3**), and since the phase transition may induce micro-cracks in the SnSe matrix, we selected the measured temperature range as 300 K – 793 K. High repeatability was realized with measured fluctuations being 10 %, 2 % and 5 % for σ, S and κ, respectively, as shown in **Figure S4**. Besides, for *p*-type SnSe, considering that hat all properties except S measured along the *bc*-axis (in-plane) are higher than that measured along the *a*-axis (out-of-plane) due to the anisotropy (shown in **Figure S5** in Supporting Information),[9, 13, 38] we chose the *bc*-axis as the main measured direction in the following discussions. **Figure 4(a)** shows the temperature-dependent σ. Compared with stoichiometric SnSe, the σ values obtained from $Sn_{1-x}Se$ single crystals are significantly improved, especially at high temperature (>750 K) due to the higher Sn vacancy concentration, which releases more holes *via* thermal activation.[3] **Figure 4(b)** exhibits the temperature-dependent S, showing that the S values of $Sn_{1-x}Se$ single crystals drop significantly at high temperatures (> 650 K), indicating an increase of p,[3, 9] fitting well with the results of σ. Peak

S values can be achieved at the bipolar-effect temperature T^*, and a shifting of T^* towards a higher T for $Sn_{1-x}Se$ also indicates an increase of p.[3, 9] **Figure 4(c)** shows the determined $S^2\sigma$, from which a high average $S^2\sigma$ of 6.06 μW cm^{-1} K^{-2} at 793 K can be secured in the $Sn_{1-x}Se$ single crystals. **Figure 4(d)** plots the calculated T-dependent κ *via* $\kappa = D \cdot C_p \cdot \rho$ [9], where the measured D and ρ values are plotted in **Figure S6(a)**, and the measured C_p is shown in **Figure S6(b)**. As can be seen, compared with stoichiometric SnSe, κ of $Sn_{1-x}Se$ single crystals is significantly decreased from room temperature to 793 K. This is because the induced Sn vacancies and thus the slightly distorted lattice can effectively scatter the phonons from short and medium wavelengths.[3, 12, 16, 24] An extra-low κ of ~0.39 W m^{-1} K^{-1} is achieved at 793 K, which is close to the results from a previous study (~0.4 W m^{-1} K^{-1} at 773 K).[13] Besides, considering the high relative densities in the single crystals (all > 98.7 %),[13, 17] the obtained κ values must be intrinsic.

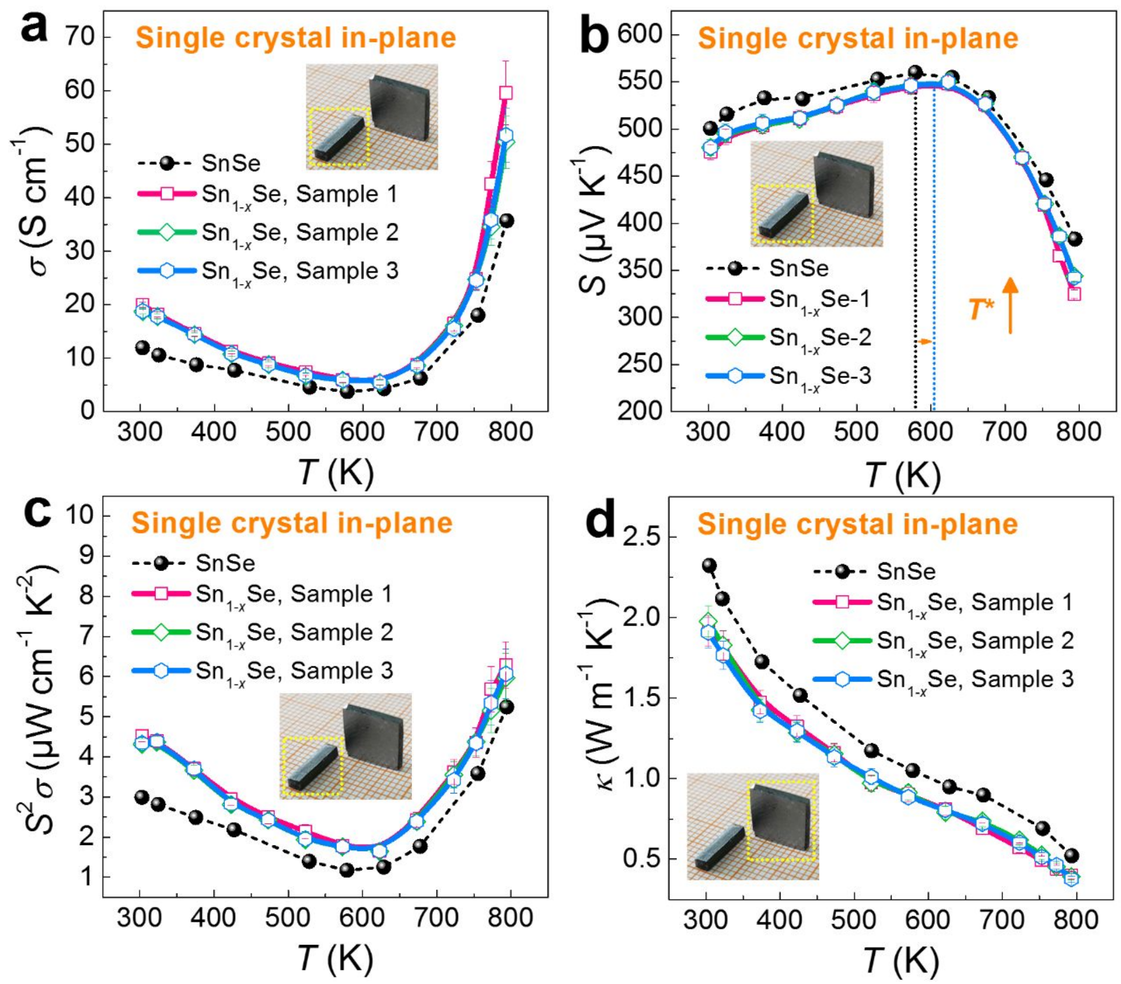

Figure 4. Plots of measured T-dependent properties from SnSe and $Sn_{1-x}Se$ single crystals along in-plane direction (bc-axis): (a) σ; (b) S; (c) $S^2\sigma$; and (d) κ.

To confirm the improved p at high temperature, we measured the temperature-dependent p, as shown in **Figure 5(a)**. As can be seen, the $Sn_{1-x}Se$ has higher p than SnSe due to the extra holes provided by the Sn vacancies. The p of $Sn_{1-x}Se$ at 793 K can reach to $>1\times10^{19}$ cm^{-3} triggered by thermal activation, and the induced ~0.3 % Sn vacancies play a significant role in producing more holes under thermal excitation, contributing to such high p values.[3] To better understand the carrier transport principles, **Figure 5(b)** plots the corresponding carrier mobility μ, which roughly follows the power law ($\mu \propto T^{d}$).[27, 35] It is seen that from room temperature to ~623 K, μ decreases roughly following $\mu \propto T^{-1.5}$, indicating that acoustic-phonon scattering dominates carrier scattering.[27, 35] However, from ~623 K to ~750 K, there is an increase of μ roughly following $\mu \propto T^{1.2}$, which should be derived from thermal excitation near the phase transition.[10] Meanwhile, $Sn_{1-x}Se$ possess lower μ than SnSe for the entire temperature range due to the crystal imperfections (mainly Sn vacancies and lattice distortions) in $Sn_{1-x}Se$, which block and/or scatter carriers and in turn impede the carrier transportation. Besides, as shown in **Figure S5**, the p is weakly dependent on the measured direction, but the μ is strongly dependent it, from which the μ along the out-of-plane is significantly lower than that along the in-plane, which is derived from the strong anisotropy of SnSe.[9, 12-13, 16, 24]

From **Figure 4(d)**, an obvious reduce of κ from 600 K to 800 K can be observed, even though there is a minor carrier activation at this temperature as shown in **Figure 5(a)**, which should result in an increase of κ due to the increase of κ_e. In fact, previous works also reported the similar results on single crystal SnSe – the κ continued to reduce from 600 K to 800 K until the phase transition at 800 K.[13-15, 20, 39] To further understand such unusual behavior, we study the contributions from electrons and lattice on the κ, and the κ_e is calculated *via* the Wiedemann–Franz law $\kappa_e = L \cdot \sigma \cdot T$,[3, 40] where L is the Lorenz number calculated from the single parabolic band (SPB) model[25-26, 41-42] as shown in **Figure 5(c)**. The calculation details can be found in **Section 7** in Supporting Information. For L, the value is relatively constant at ~1.5×10^{-8} V^2 K^{-2} in the entire temperature range.[24] **Figures 5(d)** and **5(e)** show the calculated temperature dependent κ_e and κ_l, respectively, and κ_l is obtained by subtracting the electronic contribution κ_e from κ. We find that the electron contribution is much lower than the lattice contribution, and the latter takes about 82 % of the total κ as shown in **Figure 5(f)**. We find that the κ_l shows a slower scaling with temperature (from 300 to 600 K) than the $1/T$ trend induced by phonon-phonon scattering, as shown in **Figure 5(g)**. This indicates the existence of considerable phonon-defect scattering with Sn vacancies and concomitant lattice distortions in $Sn_{1-x}Se$, which lead to low κ_l. With the temperatures above 600 K, the crystals are approaching to the phase transition regime and the κ_l goes below 0.33 W m^{-1} K^{-1} at 793 K. It should be noted that this value is close to the minimum κ_l (0.33 W m^{-1} K^{-1} along the *c*-axis and 0.36 W m^{-1} K^{-1} along the *b*-axis[13, 43]) calculated *via* a classical Debye-Cahill model[44].

Figure 5(h) exhibits the *T*-dependent *ZT*s with a high peak *ZT* of ~1.24 at 793 K observed before the phase transition, indicating that $Sn_{1-x}Se$ possesses considerable potential for thermoelectric applications.[1, 3] **Figure 5(i)** compares the measured *ZT* values with the predicted ones from the SPB model at different temperatures.[41-42, 45-46] We find that the experimental p are all located below the theoretically optimal values. Therefore, increasing p is key to improving the thermoelectric performance. In this work, the achieved high p = ~1.2×10^{19} cm^{-3} induced by the large Sn vacancy concentration is fairly close to the optimal value of 3×10^{19} cm^{-3} at 793 K, which partially explains the achieved high *ZT* of ~1.24. In the future, higher *ZT*s may be achieved by further increasing p. Besides, it should be noticed that the *ZT* value achieved at this temperature (close to phase transition) may be slightly overestimated. This is because that the C_p was measured using high temperature differential scanning calorimetry. For SnSe which is a typical anharmonic material,[3, 47-49] the discrepancy between constant-pressure specific heat C_p and constant-volume specific heat C_v is offset to the first order by a decrease in the packing density due to thermal expansion. However, this is not accurate near the phase transition temperature. Hence, it can be assumed that $C_p = C_v$ at all temperatures, except at phase transition temperature. Considering of these, this *ZT* value near the phase transition may be overestimated due to the total κ derived from the measured C_p.

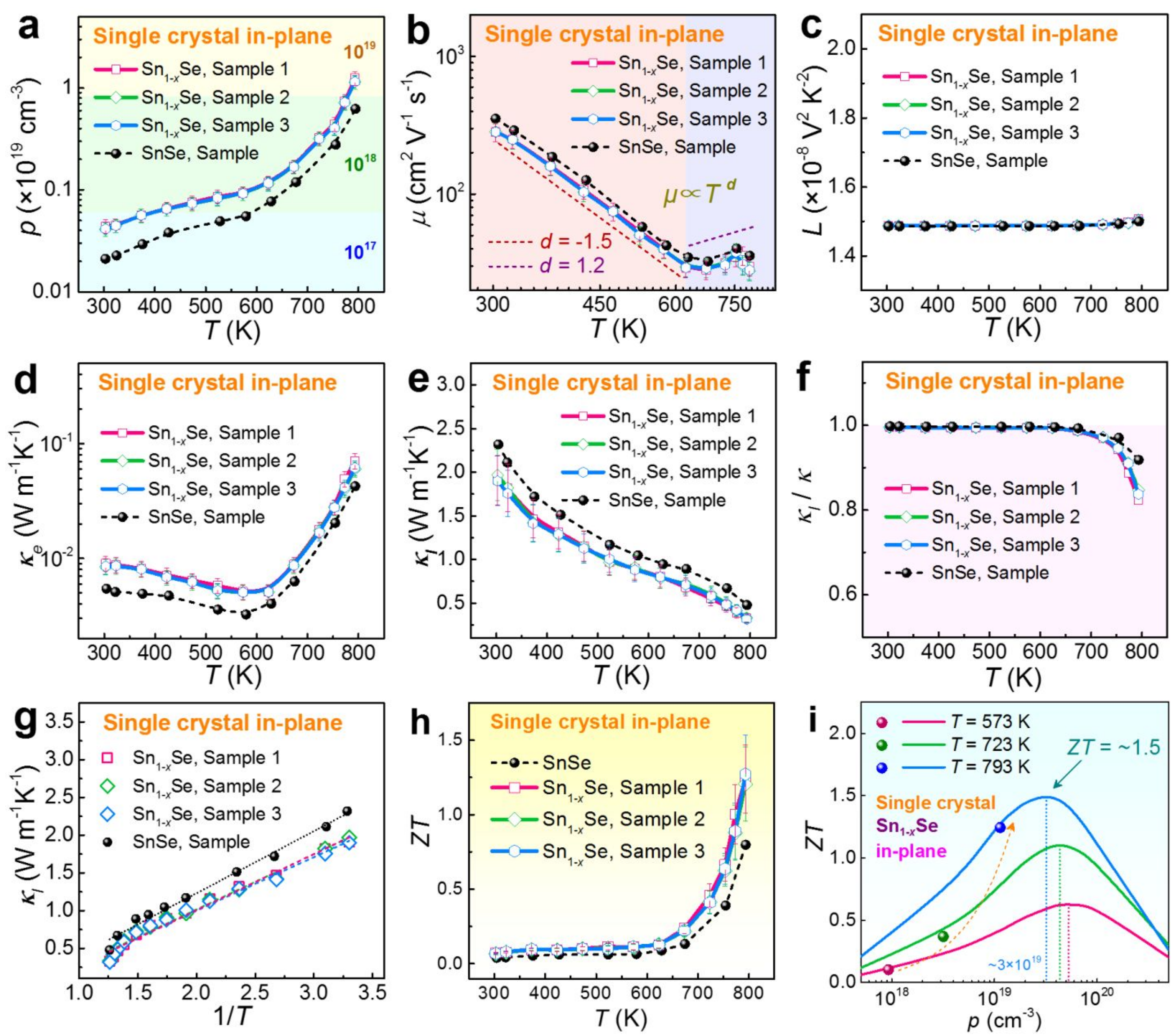

Figure 5. Extended thermoelectric properties for SnSe single crystals along in-plane direction (*bc*-axis): *T*-dependent (a) *p*; (b) μ; (c) *L*; (d) κ_e; (e) κ_l; *T*-dependent (f) κ_l/κ ratio; (g) $1/T$-dependent κ_l;

(h) *ZT* compared with stoichiometric SnSe; and (i) a comparison of achieved *ZT*s with predicted *ZT*s.

3.3 First-Principle Studies. To further understand the mechanism of the increase of *p*, we conducted density functional theory (DFT) calculations of the electronic band structures of SnSe and $Sn_{1-x}Se$, as shown in **Figure 6(a)** and **6(b)**, respectively. For SnSe and $Sn_{1-x}Se$, we used $Sn_{128}Se_{128}$ and $Sn_{127}Se_{128}$ stoichiometries, respectively, by using 2×4×4 (256 atoms) supercells. It is clear that the Fermi level moves into the valence band with the presence of a Sn vacancy in the supercell, indicating that the Sn vacancy changes SnSe into a degenerate *p*-type semiconductor with significantly increased *p*. To further unveil the impact of increasing the Sn-vacancy concentration, we also calculated the electronic band structure of $Sn_{126}Se_{128}$ and $Sn_{125}Se_{128}$ (with 2 and 3 Sn vacancies in the supercell, respectively). The densities of states (DOS) of $Sn_{128}Se_{128}$, $Sn_{127}Se_{128}$, $Sn_{126}Se_{128}$ and $Sn_{125}Se_{128}$ are compared in **Figure 6(c)**, in which it is seen that the Fermi level moves more deeply into the valence band with increasing Sn vacancies. Therefore, the calculations clearly demonstrate that the Sn vacancies contribute to the increased *p* and in turn an enhanced $S^2\sigma$, agreeing with the experimental results shown in **Figure 4**.[50-52] **Figure 6(d)** shows the measured band gaps of SnSe and $Sn_{1-x}Se$ at room temperature (α-SnSe), which show that the band gap increases after introducing Sn vacancies but the increment is negligibly (from ~0.965 eV to ~0.975 eV). Although DFT calculations are well known for the underestimation of band gaps,[53-54] we find that they predict the same trend as what we measured, i.e., the band gap increases negligibly with increasing Sn vacancies. The measured band gap values are consistent with the previously reported values of ~0.9 eV.[3] The calculated effective mass (m^*) value *via* the SPB model is ~1.11 m_0 (shown in **Figure S7**), which is also close to the previously reported values.[3, 24] These results indicate that SnSe is a typical narrow-gap semiconductor with promising thermoelectric properties. The difference between the experimental and theoretical calculated p for $Sn_{1-x}Se$ can be seen in **Figure S8**.

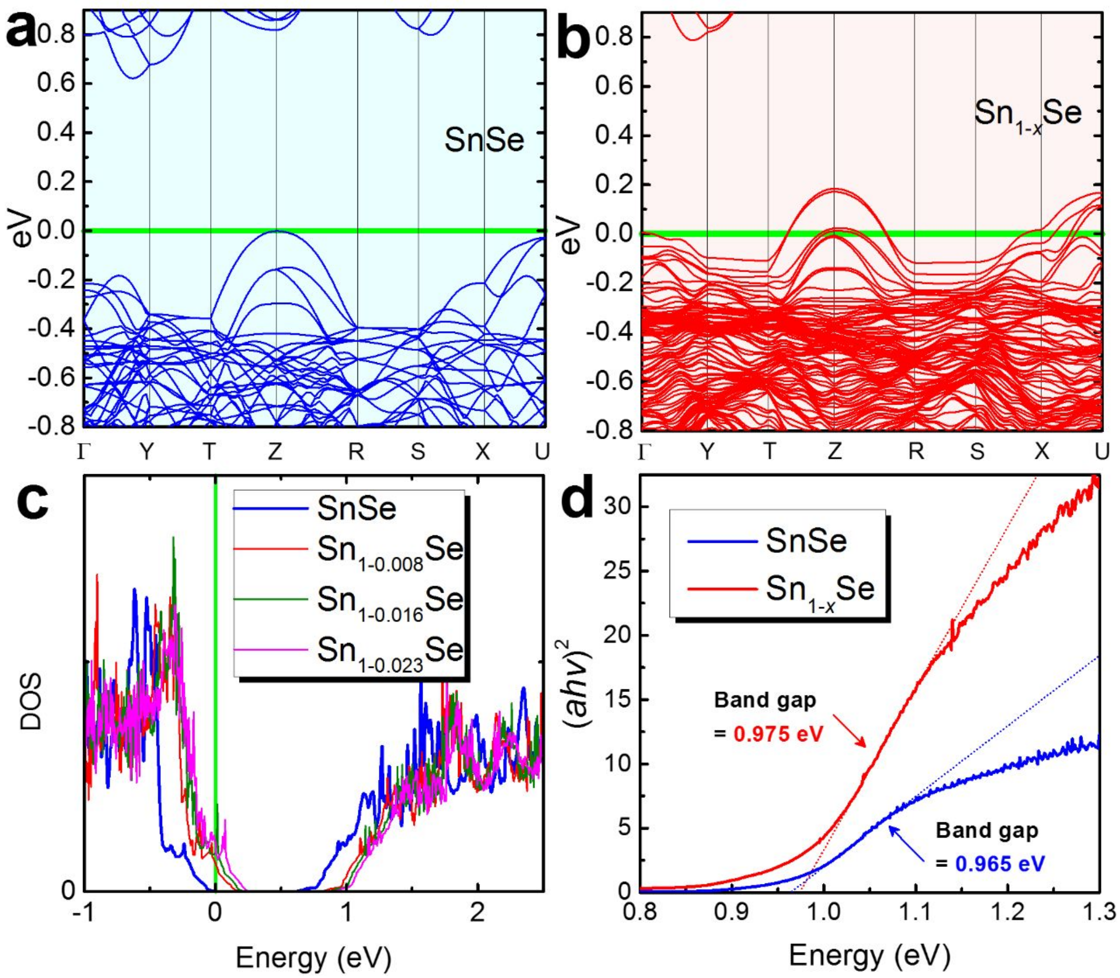

Figure 6. Comparisons of calculated band structures for (a) SnSe and (b) $Sn_{1-x}Se$; and comparisons of (c) DOS and (d) measured band gap values of SnSe and $Sn_{1-x}Se$.

Considering the significance of Sn vacancy on the enhancement of thermoelectric performance, there are some potential routes to further enhance the Sn vacancy concentration in the SnSe matrix, including adjusting the synthesis temperature as well as the synthesis time to alter the reaction kinetics and in turn produce more Sn vacancies,[3] which need further experiments to demonstrate. Meanwhile, there are also considerable potentials to further improve the thermoelectric properties *via* proper band engineering such as doping.[3, 39] Besides, it should be noticed that there could be mechanical stability issues for a device when employing single crystal SnSe. Considering the changes in lattice parameters as a function of temperature near the displacive phase transition, especially arising from the negative thermal expansion along the *c*-axis, the phase transition may lead to electrical contact issues in the thermoelectric legs of the device itself. This is why we avoid to measure the thermoelectric properties over the phase transition temperature at 800 K.

4. CONCLUSIONS

In conclusion, we fabricated large-size off-stoichiometric SnSe single crystals with a Sn vacancy level of ~0.3 % *via* an improved horizontal Bridgman method for the first time. The grown single crystals have a super large size of ~70 mm×50 mm×15 mm with a weight of 148 g and a record-high mass density >6.1 g cm^{-3}. A competitive ZT of ~1.24 is achieved at 793 K owing to the enhanced power factor as well as the reduced lattice thermal conductivity. This work provides a new perspective in achieving excellent thermoelectric properties of SnSe.

ASSOCIATED CONTENT

Supporting information.

The Supporting Information is available free of charge on the ACS Publications website at DOI:

Sn-Se phase diagram, XRD and SEM results for polycrystalline SnSe, TG curves of products, reproducibility and anisotropy of thermoelectric performance, measured *D* and C_p, calculated *m** *via* SPB model with detailed calculations, and calculated theoretical *p via* DFT. (PDF).

AUTHOR INFORMATION

[1] These authors contributed equally to this work.

Corresponding Author

* Email: zhigang.chen@usq.edu.au (ZGC); zhigang.chen@uq.edu.au (ZGC);

* Email: j.zou@uq.edu.au (JZ);

* Email: jmaish@aliyun.com (MJ).

Notes

The authors declare no competing financial interest.

ACKNOWLEDGMENT

This work was financially supported by Public Projects of Zhejiang Province (2017C31006), National Natural Science Foundation of China (Grant No. 51809161), Shanghai Municipal Natural

Science Foundation (Grant No.18ZR1416000), and Australian Research Council. XLS thanks the IPRS for providing his PhD program. We acknowledge Doc. YZ and LSQ for Hall measurement, and ZWC for discussion. The Australian Microscopy & Microanalysis Research Facility is acknowledged for providing characterization facilities. Theoretical work by TLF and STP is supported in part by Department of Energy grant DE-FG0209ER46554 and by the McMinn Endowment. Computations at Vanderbilt University and ORNL were performed at the National Energy Research Scientific Computing Center (NERSC), a Department of Energy, Office of Science, User Facility funded through Contract No. DE-AC02-05CH11231. Computations also used the Extreme Science and Engineering Discovery Environment (XSEDE).

Reference

(1) Zhu, T.; Liu, Y.; Fu, C.; Heremans, J. P.; Snyder, J. G.; Zhao, X. Compromise and Synergy in High‐Efficiency Thermoelectric Materials. *Adv. Mater.* **2017**, *29*, 1605884.

(2) Zhao, L.-D.; Dravid, V. P.; Kanatzidis, M. G. The Panoscopic Approach to High Performance Thermoelectrics. *Energy Environ. Sci.* **2014**, *7*, 251-268.

(3) Chen, Z.-G.; Shi, X.; Zhao, L.-D.; Zou, J. High-Performance SnSe Thermoelectric Materials: Progress and Future Challenge. *Prog. Mater. Sci.* **2018**, *97*, 283-346.

(4) Yang, L.; Chen, Z.-G.; Dargusch, M. S.; Zou, J. High Performance Thermoelectric Materials: Progress and Their Applications. *Adv. Energy Mater.* **2017**, *8*, 1701797.

(5) Zhao, K.; Duan, H.; Raghavendra, N.; Qiu, P.; Zeng, Y.; Zhang, W.; Yang, J.; Shi, X.; Chen, L. Solid‐State Explosive Reaction for Nanoporous Bulk Thermoelectric Materials. *Adv. Mater.* **2017**, *29*, 1701148.

(6) Dresselhaus, M. S.; Chen, G.; Tang, M. Y.; Yang, R. G.; Lee, H.; Wang, D. Z.; Ren, Z. F.; Fleurial, J. P.; Gogna, P. New Directions for Low-Dimensional Thermoelectric Materials. *Adv. Mater.* **2007**, *19*, 1043-1053.

(7) Moshwan, R.; Yang, L.; Zou, J.; Chen, Z.-G. Eco-friendly SnTe Thermoelectric Materials: Progress and Future Challenge. *Adv. Funct. Mater.* **2017**, *27*, 1703278.

(8) Liu, W. D.; Chen, Z. G.; Zou, J. Eco‐Friendly Higher Manganese Silicide Thermoelectric Materials: Progress and Future Challenges. *Adv. Energy Mater.* **2018**, 1800056.

(9) Shi, X.; Chen, Z.; Liu, W.; Yang, L.; Hong, M.; Moshwan, R.; Huang, L.; Zou, J. Achieving High Figure of Merit in *p*-Type Polycrystalline $Sn_{0.98}Se$ *via* Self-Doping and Anisotropy-Strengthening. *Energy Storage Mater.* **2018**, *10*, 130-138.

(10) Jin, M.; Chen, Z.; Tan, X.; Shao, H.; Liu, G.; Hu, H.; Xu, J.; Yu, B.; Shen, H.; Xu, J. Charge Transport in Thermoelectric SnSe Single Crystals. *ACS Energy Lett.* **2018**, *3*, 689-694.

(11) Chen, Z.-G.; Han, G.; Yang, L.; Cheng, L.; Zou, J. Nanostructured Thermoelectric Materials: Current Research and Future Challenge. *Prog. Nat. Sci.* **2012**, *22*, 535-549.

(12) Shi, X. L.; Zheng, K.; Liu, W. D.; Wang, Y.; Yang, Y. Z.; Chen, Z. G.; Zou, J. Realizing High Thermoelectric Performance in *n*‐Type Highly Distorted Sb‐Doped SnSe Microplates *via* Tuning High Electron Concentration and Inducing Intensive Crystal Defects. *Adv. Energy Mater.* **2018**, *8*, 1800775.

(13) Zhao, L. D.; Lo, S. H.; Zhang, Y.; Sun, H.; Tan, G.; Uher, C.; Wolverton, C.; Dravid, V. P.; Kanatzidis, M. G. Ultralow Thermal Conductivity and High Thermoelectric Figure of Merit in SnSe Crystals. *Nature* **2014**, *508*, 373-377.

(14) Chang, C.; Wu, M.; He, D.; Pei, Y.; Wu, C.-F.; Wu, X.; Yu, H.; Zhu, F.; Wang, K.; Chen, Y. 3D Charge and 2D Phonon Transports Leading to High Out-of-Plane *ZT* in *n*-Type SnSe Crystals. *Science* **2018**, *360*, 778-783.

(15) Peng, K.; Lu, X.; Zhan, H.; Hui, S.; Tang, X.; Wang, G.; Dai, J.; Uher, C.; Wang, G.; Zhou, X. Broad Temperature Plateau for High *ZT*s in Heavily Doped *p*-Type SnSe Single Crystals. *Energy Environ. Sci.* **2016**, *9*, 454-460.

(16) Shi, X. L.; Zheng, K.; Hong, M.; Liu, W. D.; Moshwan, R.; Wang, Y.; Qu, X.-L.; Chen, Z. G.; Zou, J. Boosting the Thermoelectric Performance of *p*-Type Heavily Cu-doped Polycrystalline SnSe *via* Inducing Intensive Crystal Imperfections and Defect Phonon Scattering. *Chem. Sci.* **2018**, *9*, 7376-7389.

(17) Wei, P.-C.; Bhattacharya, S.; He, J.; Neeleshwar, S.; Podila, R.; Chen, Y.; Rao, A. The Intrinsic Thermal Conductivity of SnSe. *Nature* **2016**, *539*, E1-E2.

(18) Ibrahim, D.; Vaney, J.-B.; Sassi, S.; Candolfi, C.; Ohorodniichuk, V.; Levinsky, P.; Semprimoschnig, C.; Dauscher, A.; Lenoir, B. Reinvestigation of the Thermal Properties of Single-Crystalline SnSe. *Appl. Phys. Lett.* **2017**, *110*, 032103.

(19) Jin, M.; Shao, H.; Hu, H.; Li, D.; Shen, H.; Xu, J.; Jiang, J. Growth and Characterization of Large Size Undoped *p*-Type SnSe Single Crystal by Horizontal Bridgman Method. *J. Alloy. Compd.* **2017**, *712*, 857-862.

(20) Duong, A. T.; Nguyen, V. Q.; Duvjir, G.; Duong, V. T.; Kwon, S.; Song, J. Y.; Lee, J. K.; Lee, J. E.; Park, S.; Min, T.; Lee, J.; Kim, J. Achieving *ZT* = 2.2 with Bi-doped *n*-Type SnSe Single Crystals. *Nat. Commun.* **2016**, *7*, 13713.

(21) He, J.; Tan, X.; Xu, J.; Liu, G.-Q.; Shao, H.; Fu, Y.; Wang, X.; Liu, Z.; Xu, J.; Jiang, H. Valence Band Engineering and Thermoelectric Performance Optimization in SnTe by Mn-Alloying *via* a Zone-Melting Method. *J. Mater. Chem. A* **2015**, *3*, 19974-19979.

(22) Sist, M.; Zhang, J.; Brummerstedt Iversen, B. Crystal Structure and Phase Transition of Thermoelectric SnSe. *Acta Crystallogr. B* **2016**, *72*, 310-316.

(23) Wei, W.; Chang, C.; Yang, T.; Liu, J.; Tang, H.; Zhang, J.; Li, Y.; Xu, F.; Zhang, Z.; Li, J.-F. Achieving High Thermoelectric Figure of Merit in Polycrystalline SnSe *via* Introducing Sn Vacancies. *J. Am. Chem. Soc.* **2017**, *140*, 499-505.

(24) Shi, X.; Wu, A.; Liu, W.; Moshwan, R.; Wang, Y.; Chen, Z.-G.; Zou, J. Polycrystalline SnSe with Extraordinary Thermoelectric Property *via* Nanoporous Design. *ACS Nano* **2018**, *12*, 11417-11425.

(25) Liu, W.; Shi, X.; Hong, M.; Yang, L.; Moshwan, R.; Chen, Z.-G.; Zou, J. Ag Doping Induced Abnormal Lattice Thermal Conductivity in Cu_2Se. *J. Mater. Chem. C* **2018**, *6*, 13225-13231.

(26) Liu, W.; Shi, X.; Moshwan, R.; Hong, M.; Yang, L.; Chen, Z.-G.; Zou, J. Enhancing Thermoelectric Performance of $(Cu_{1-x}Ag_x)_2Se$ *via* CuAgSe Secondary Phase and Porous Design. *Sustain*. *Mater. Tech*. **2018**, *17*, e00076.

(27) Nassary, M. The Electrical Conduction Mechanisms and Thermoelectric Power of SnSe Single Crystals. *Turk. J. Phys.* **2009**, *33*, 201-208.

(28) Wang, S.; Hui, S.; Peng, K.; Bailey, T. P.; Liu, W.; Yan, Y.; Zhou, X.; Tang, X.; Uher, C. Low Temperature Thermoelectric Properties of *p*-Type Doped Single-Crystalline SnSe. *Appl. Phys. Lett.* **2018**, *112*, 142102.

(29) Kresse, G.; Hafner, J. *Ab initio* Molecular Dynamics for Liquid Metals. *Phys. Rev. B* **1993**, *47*, 558.

(30) Kresse, G.; Furthmüller, J. Efficient Iterative Schemes for *ab initio* Total-Energy Calculations Using a Plane-Wave Basis Set. *Phys. Rev. B* **1996**, *54*, 11169.

(31) Perdew, J. P.; Burke, K.; Ernzerhof, M. Generalized Gradient Approximation Made Simple. *Phys. Rev. Lett.* **1996**, *77*, 3865.

(32) Gao, J.; Zhu, H.; Mao, T.; Zhang, L.; Di, J.; Xu, G. The Effect of Sm Doping on the Transport and Thermoelectric Properties of SnSe. *Mater. Res. Bull.* **2017**, *93*, 366-372.

(33) Jin, M.; Shao, H.; Hu, H.; Li, D.; Xu, J.; Liu, G.; Shen, H.; Xu, J.; Jiang, H.; Jiang, J. Single Crystal Growth of $Sn_{0.97}Ag_{0.03}Se$ by a Novel Horizontal Bridgman Method and its Thermoelectric Properties. *J. Cryst. Growth* **2017**, *460*, 112-116.

(34) Ma, X.-H.; Cho, K.-H.; Sung, Y.-M. Growth Mechanism of Vertically Aligned SnSe Nanosheets *via* Physical Vapour Deposition. *CrystEngComm* **2014**, *16*, 5080-5086.

(35) Li, Y.; Li, F.; Dong, J.; Ge, Z.; Kang, F.; He, J.; Du, H.; Li, B.; Li, J.-F. Enhanced Mid-Temperature Thermoelectric Performance of Textured SnSe Polycrystals Made of Solvothermally Synthesized Powders. *J. Mater. Chem. C* **2016**, *4*, 2047-2055.

(36) Kim, S.-u.; Duong, A.-T.; Cho, S.; Rhim, S. H.; Kim, J. A Microscopic Study Investigating the Structure of SnSe Surfaces. *Surf. Sci.* **2016**, *651*, 5-9.

(37) Duvjir, G.; Min, T.; Thi Ly, T.; Kim, T.; Duong, A.-T.; Cho, S.; Rhim, S.; Lee, J.; Kim, J. Origin of *p*-Type Characteristics in a SnSe Single Crystal. *Appl. Phys. Lett.* **2017**, *110*, 262106.

(38) Chang, C.; Zhao, L.-D. Anharmoncity and Low Thermal Conductivity in Thermoelectrics. *Mater*. *Today Phys*. **2018**, *4*, 50-57.

(39) Zhao, L.-D.; Tan, G.; Hao, S.; He, J.; Pei, Y.; Chi, H.; Wang, H.; Gong, S.; Xu, H.; Dravid, V. P. Ultrahigh Power Factor and Thermoelectric Performance in Hole-Doped Single-Crystal SnSe. *Science* **2016**, *351*, 141-144.

(40) Moshwan, R.; Shi, X.-L.; Liu, W.-D.; Yang, L.; Wang, Y.; Hong, M.; Auchterlonie, G.; Zou, J.; Chen, Z.-G. High Thermoelectric Performance in Sintered Octahedron-Shaped Sn $(CdIn)_xTe_{1+2x}$ Microcrystals. *ACS Appl. Mater. Interf.* **2018**, *10*, 38944-38952.

(41) Xu, Y.; Li, W.; Wang, C.; Li, J.; Chen, Z.; Lin, S.; Chen, Y.; Pei, Y. Performance Optimization and Single Parabolic Band Behavior of Thermoelectric MnTe. *J. Mater. Chem. A* **2017**, *5*, 19143-19150.

(42) Shen, J.; Chen, Z.; lin, S.; Zheng, L.; Li, W.; Pei, Y. Single Parabolic Band Behavior of Thermoelectric *p*-Type CuGaTe2. *J. Mater*. *Chem*. *C* **2016**, *4*, 209-214.

(43) Yang, J.; Zhang, G.; Yang, G.; Wang, C.; Wang, Y. X. Outstanding Thermoelectric Performances for both *p*- and *n*-Type SnSe from First-Principles Study. *J. Alloy. Compd.* **2015**, *644*, 615-620.

(44) Cahill, D. G.; Watson, S. K.; Pohl, R. O. Lower Limit to the Thermal Conductivity of Disordered Crystals. *Phys. Rev. B* **1992**, *46*, 6131.

(45) She, X.; Su, X.; Du, H.; Liang, T.; Zheng, G.; Yan, Y.; Akram, R.; Uher, C.; Tang, X. High Thermoelectric Performance of Higher Manganese Silicides Prepared by Ultra-Fast Thermal Explosion. *J. Mater. Chem. C* **2015**, *3*, 12116-12122.

(46) Zhao, L.; Islam, S. M. K. N.; Wang, J.; Cortie, D. L.; Wang, X.; Cheng, Z.; Wang, J.; Ye, N.; Dou, S.; Shi, X.; Chen, L.; Snyder, G. J.; Wang, X. Significant Enhancement of Figure-of-Merit in Carbon-Reinforced Cu_2Se Nanocrystalline Solids. *Nano Energy* **2017**, *41*, 164-171.

(47) Delaire, O. Phonon Scattering in Thermoelectrics: Thermal Transport, Strong Anharmonicity, and Emergent Quasiparticles. *Bull. Am. Phys. Soc.* **2017**, *62*.

(48) Hong, J.; Delaire, O. Electronic Instability and Anharmonicity in SnSe. *Cond. Mat. Mtrl. Sci.* **2016**, 1604.07077.

(49) Tang, G.; Liu, J.; Zhang, J.; Li, D.; Rara, K. H.; Xu, R.; Lu, W.; Liu, J.; Zhang, Y.; Feng, Z. Realizing High Thermoelectric Performance below Phase Transition Temperature in Polycrystalline SnSe *via* Lattice Anharmonicity Strengthening and Strain Engineering. *ACS Appl. Mater. Interf.* **2018**, *10*, 30558-30565.

(50) Hong, M.; Chen, Z.-G.; Pei, Y.; Yang, L.; Zou, J. Limit of *ZT* Enhancement in Rocksalt Structured Chalcogenides by Band Convergence. *Phys. Rev. B* **2016**, *94*, 161201.

(51) Lv, H.; Lu, W.; Shao, D.; Sun, Y. Enhanced Thermoelectric Performance of Phosphorene by Strain-Induced Band Convergence. *Phys. Rev. B* **2014**, *90*, 085433.

(52) Pei, Y.; Shi, X.; LaLonde, A.; Wang, H.; Chen, L.; Snyder, G. J. Convergence of Electronic Bands for High Performance Bulk Thermoelectrics. *Nature* **2011**, *473*, 66-69.

(53) Hong, M.; Chasapis, T.C.; Chen, Z.-G.; Yang, L.; Kanatzidis, M.G.; Snyder, G.J.; Zou, J. *n*-Type $Bi_2Te_{3-x}Se_x$ Nanoplates with Enhanced Thermoelectric Efficiency Driven by Wide-Frequency Phonon Scatterings and Synergistic Carrier Scatterings. *ACS Nano* **2016**, *10*, 4719-4727.

(54) Shi, X.; Wu, A.; Feng, T.; Zheng, K.; Liu, W.; Sun, Q.; Hong, M.; Pantelides, S.T.; Chen, Z.-G.; Zou, J. High Thermoelectric Performance in *p*-Type Polycrystalline Cd-Doped SnSe Achieved by a Combination of Cation Vacancies and Localized Lattice Engineering. *Adv*. *Energy Mater*. **2019**, DOI: 10.1002/aenm.201803242.

TOC GRAPHICS